Journal of Materials Chemistry A

ROYAL SOCIETY OF CHEMISTRY

PAPER

View Article Online
View Journal | View Issue

Check for updates

Cite this: J. Mater. Chem. A, 2026, 14, 15097

Defect-surface engineering of La-doped ceria for microwave-assisted hydrogen production

Aitor Domínguez-Saldaña, [a] Laura Navarrete,[a] Alfonso J. Carrillo, [a] Maria Balaguer, [a] Joaquin Santos,[c] Beatriz García-Baños, [b] Pedro Plaza-González,[b] David Catalán-Martínez,[a] Jose M. Catalá-Civera *[b] and Jose M. Serra *[a]

Hydrogen plays a pivotal role in decarbonizing the energy and chemical sectors, yet current production methods are limited by high temperatures and energy demands. Microwave-assisted thermochemical redox cycles offer a promising low-temperature, contactless alternative by coupling electromagnetic energy with reducible oxides. In this study, we explore La-doped ceria ($Ce_{1-x}La_xO_{2-\delta}$) as a tunable platform to enhance microwave-driven hydrogen production. We demonstrate that introducing La^{3+} into the ceria lattice reduces the bandgap and increases dielectric permittivity, enabling Ce^{4+} to Ce^{3+} reduction at temperatures as low as 110 °C. Among the series, $Ce_{0.9}La_{0.1}O_{1.95}$ exhibits optimal performance, balancing high ionic mobility and microwave absorption. Combined with tailored surface area, this composition achieves an unprecedented hydrogen production rate of 2.60 mL g^{-1} per cycle at temperatures below 400 °C. Correlations between dopant concentration, polarization behavior, and redox kinetics reveal the key role of band structure breakdown and defect formation in driving non-equilibrium reduction. Our findings uncover mechanistic insights into microwave–material interactions and establish design principles for next-generation redox materials. This approach provides a framework for scalable, electrified hydrogen production *via* electronic structure and defect engineering in oxide systems.

Received 18th September 2025
Accepted 15th December 2025

DOI: 10.1039/d5ta07647a

rsc.li/materials-a

Open Access Article. Published on 10 maart 2026. Downloaded on 27-4-2026 02:35:05.
This article is licensed under a Creative Commons Attribution-NonCommercial 3.0 Unported Licence.

Introduction

Implementing renewable energy sources is crucial for the transition away from a fossil-fuel-based economy. Due to the intermittent nature of these resources, developing robust energy storage and conversion technologies is essential.[1–3] In this context, green hydrogen is emerging as a key energy carrier,[4–7] enabling chemical storage of renewable electricity for use during demand peaks or low generation periods.

Among available technologies, thermochemical redox cycles have attracted growing interest for green hydrogen production due to their ability to deliver high-purity H_2 in a two-step operation without requiring downstream separation.[8–14] These cycles proceed *via* an initial high-temperature endothermic reduction step, in which oxygen is released from a metal oxide lattice, creating oxygen vacancies ($V_O^{\cdot\cdot}$). A subsequent exothermic oxidation step in the presence of H_2O refills these vacancies, releasing hydrogen.[15–17] Cerium dioxide (CeO_2) remains the state-of-the-art material for these cycles, owing to its robust redox stability, fast oxygen exchange kinetics, and favorable thermodynamics.[10,18,19] However, conventional thermochemical approaches require temperatures exceeding 1400 °C to activate ceria-based oxides, which impose serious challenges for materials, energy efficiency, and reactor design.[10,19,20]

Microwave-assisted technology offers advantages such as contactless and volumetric energy transfer to dielectrics with rapid and selective activation of redox-active oxides.[21–27] The thermodynamics of this process closely resemble those of steam electrolysis and could potentially achieve similar energy efficiency levels as solid-oxide electrolysis.[21] In microwave-driven redox cycles, materials undergo cyclic exposure to electromagnetic fields (MW ON) and subsequent oxidation (MW OFF). During the MW ON phase, dielectric materials absorb microwave energy, which drives spontaneous reduction by inducing dielectric breakdown and oxygen vacancy formation.[21,22] The onset of reduction is typically triggered upon reaching a critical threshold power (P_{th}) and induction temperature (T_i), above which polarization and charge displacement within the oxide lattice lead to significant increases in electronic conductivity.[22,28] This transition involves electronic excitation from O^{2-} 2p valence orbitals to Ce 4f conduction states,[20,22] accompanied by formation of Ce^{3+} and polarons,[21,22,29,30] which also promote

[a]Instituto de Tecnología Química, (Universitat Politècnica de València-Consejo Superior de Investigaciones Científicas), Valencia, Spain. E-mail: jmserra@itq.upv.es
[b]Instituto ITACA, (Universitat Politècnica de València), Valencia, Spain. E-mail: jmcatala@dcom.upv.es
[c]Universidad Europea de Valencia, Paseo de la Alameda 7, 46010, Valencia, Spain

Open Access Article. Published on 10 maart 2026. Downloaded on 27-4-2026 02:35:05.
This article is licensed under a Creative Commons Attribution-NonCommercial 3.0 Unported Licence.

rapid heating. Once the material reaches ~400 °C, the microwaves are turned off, and the material undergoes oxidation with water vapor, regenerating Ce^{4+} and producing H_2.[22,31] Notably, because this redox behavior is surface-limited at these lower temperatures, the rapid reduction-oxidation response is strongly dependent on the oxide's textural properties.[21,22]

Previous studies have demonstrated that aliovalent doping of ceria with trivalent cations such as La^{3+}, Gd^{3+}, and Y^{3+} enhances redox performance under both thermal and microwave conditions by expanding the lattice, lowering the reduction enthalpy, and increasing oxygen mobility through steric and coulombic effects that promote vacancy formation and diffusion.[22,30,32–34] Beyond ionic transport, recent investigations reveal that the microwave response of doped ceria is governed by a synergistic interplay between defect chemistry, dielectric polarization, and electronic structure.[22,24,32] Acceptor-type dopants such as La^{3+} and Gd^{3+} not only enhance ionic conductivity but also introduce localized defect states and reduce the bandgap, thereby facilitating non-equilibrium electronic transitions and accelerating Ce^{4+} reduction under microwave fields. In contrast, donor-type dopants (*e.g.*, Nb^{5+}) stabilize the electronic structure and suppress charge delocalization, mitigating thermal runaway effects.[35] These phenomena are consistent with the microwave-induced breakdown of the band structure, which promotes oxygen vacancy formation and rapid redox cycling. Furthermore, the effect of surface area is critical,[34] as microwave-induced reduction is spatially localized and surface-limited, making high-area, small-grained materials particularly effective in amplifying O_2 and H_2 evolution.[24] Together, these insights highlight the need for simultaneous control over defect landscapes and electronic structure to optimize microwave-driven redox processes.

In this work, we systematically investigate La-doped ceria ($Ce_{1-x}La_xO_{2-\delta}$) as a model system to elucidate how trivalent doping and surface modification influence redox kinetics, dielectric response, and hydrogen yield under microwave excitation. By correlating structural, textural, and electronic descriptors with redox performance, we identify $Ce_{0.9}La_{0.1}O_{1.95}$ as the optimal composition, capable of reaching high reduction reactivity at low induction temperatures (~110 °C) with high H_2 production rates. These findings offer a clear path toward the rational design of next-generation redox materials for electrified water splitting, where performance is governed by the synergy between microwave–material interaction and defect-mediated reactivity.

Experimental methods

Materials preparation

The $Ce_{1-x}La_xO_{2-\delta}$ (x = 0.05, 0.10, 0.15, 0.20, 0.25, and 0.30) materials were synthesized using a coprecipitation method. This involved the use of $Ce(NO_3)_3 \cdot 6H_2O$ (99.5% purity, Alfa Aesar) and $La(NO_3)_3 \cdot 6H_2O$ (99% purity, Merck Life Science S. L.) as metallic precursors. The nitrates were dissolved in distilled water at a concentration of 0.5 M while stirring continuously at 60 °C. Once the nitrates were dissolved entirely, precipitation was initiated by adding a 0.75 M solution of $(NH_4)_2CO_3$ (≥30% NH_3 basis, Merck Life Science S. L. U.) to the precursor solution. After the solids precipitated, the resulting suspensions were vacuum filtered, dried overnight, and then calcined in air at temperatures between 600 and 1400 °C for 5 hours to obtain the desired fluorite crystal structure.

Physicochemical characterization

The synthesized materials were characterized using various techniques to obtain their structural, morphological, and electronic properties. X-ray diffraction (XRD) analysis was performed using a PANalytical Cubix fast diffractometer with CuKα1,2 radiation and an X'Celerator detector in Bragg–Brentano geometry. Diffractograms were obtained by scanning the 2θ values from 15 to 100° and were analyzed using the X'Pert HighScore Plus software. Furthermore, the size of the crystalline domain of the materials was calculated by the Scherrer equation.[36] Additionally, the microstructure of the materials was characterized using Field Emission Scanning Electron Microscopy (FESEM) with a ZEISS ULTRA 55.

The BET specific surface area of the as-synthesized materials was determined from the corresponding N_2 adsorption–desorption isotherms obtained at 77 K using a Micromeritics ASAP 2000 system. Before the adsorption measurements, the samples were outgassed at 473 K for 10 h.

UV-vis diffuse reflectance spectroscopy was employed to determine the bandgap between the valence and conduction bands of the semiconductor materials. Optical absorption was measured in the 800 to 190 nm range using a Varian 5000 UV-vis-NIR spectrophotometer in diffuse reflectance mode at room temperature. The Kubelka–Munk transformation method was applied to calculate the bandgap, using $BaSO_4$ as the reference material.

X-ray photoelectron spectroscopy (XPS) was conducted to analyze modifications in the surface oxidation state of the materials. A SPECS spectrometer with an MCD-9 detector and a non-monochromatic Al K X-ray source was utilized. The resulting spectra were processed using the CASAXPS software. The 1s orbital of adventitious carbon was used to correct the binding energy in the XPS spectra.

Microwave equipment

Microwave irradiation of doped cerias was conducted using a custom-designed cylindrical microwave cavity operating at a frequency of 2.45 GHz in the transverse electric mode (Fig. S1). The ceria-doped particles were placed on top of a frit membrane inside a tubular quartz reactor, occupying a volume with a diameter of 9.8 inches and a height of 15 mm. The reactor was positioned at the center of the microwave cavity through open apertures at the top and bottom, allowing for precise and controlled irradiation. High-power microwaves were supplied by a 120 W solid-state microwave amplifier (RCA2026U50, RFcore Ltd), which operated between 2.2 and 2.6 GHz. This was driven by the oscillator and receiver of a network analyzer (Rohde & Schwarz ZVRE) and a control system. The microwave control system employed a variable penetration coupling device and a dual directional coupler (Meca Electronics, model 722-40

 This journal is © The Royal Society of Chemistry 2026

Open Access Article. Published on 10 maart 2026. Downloaded on 27-4-2026 02:35:05.
This article is licensed under a Creative Commons Attribution-NonCommercial 3.0 Unported Licence.

– 1950 W) to measure and adjust the reflected and transmitted signals to the microwave cavity based on frequency and temperature. This setup enables achieving temperatures higher than 1000 °C in the sample under various gas atmospheres. The cavity also features additional open apertures in the side and bottom walls for positioning coupling antennas for microwave irradiation and process monitoring. To determine the material's bulk temperature, the quartz reactor's surface temperature was measured using an IR pyrometer (Optris CT – Laser LT). A mass spectrometer (Omnistar Balzers) was attached to the side of the tubular quartz reactor to analyze the exhaust gas composition during the experiments.

In this setup, materials sieved to sizes between 200 and 250 μm were reduced in a synthetic air or nitrogen atmosphere by applying microwave power in the 80 to 90 W g^{-1} range. The microwave irradiation was halted once the temperature reached 400 °C, and the materials were allowed to cool down to room temperature.

Measuring the conductivity of the sample by MCPT and DC

The conductivity of doped ceria materials was measured at both microwave frequencies (AC) and direct current (DC). For high-frequency measurements, a second low-power microwave setup (Hewlett Packard HP8720E) was positioned at the bottom of the microwave cavity to operate in the TM010 transverse magnetic mode within the frequency range of 1.9–2.2 GHz. This orthonormal configuration and a cross-coupling isolation filter minimize interference from irradiation signals. The complex permittivity (which includes the dielectric constant and loss factor) and conductivity of the materials were calculated using the microwave cavity perturbation technique (MCPT). This technique involved dynamic measurements of the microwave cavity's resonant frequency and quality factor while the samples were irradiated.

Four-point direct current measurements (DC) were also conducted to isolate the effects of the materials' interaction with microwave radiation on conductivity. To prepare the samples, the materials were pressed at 80 MPa and calcined at 1480 °C. Electrical contacts were established using silver wire and paste. Conductivity measurements were performed in a controlled synthetic air environment at temperatures ranging from 100 to 700 °C, with a 1 K min^{-1} cooling rate. The current was supplied by a programmable current source (Keithley 2601).

Material's polarizability calculation

The polarizability of the materials was calculated with the Clausius–Mossotti equation (eqn (1)) from measurements of the dielectric constant at different temperatures.

$$\frac{\varepsilon' - 1}{\varepsilon' + 2} = \frac{4\pi}{3} \cdot \frac{\alpha_m}{\varepsilon_0 V} \quad (1)$$

where α_m is the macroscopic polarizability, also termed the polarization volume, V is the lattice volume of the cubic crystal cell, ε' is the relative dielectric constant, and ε_0 is the vacuum permittivity.[37,38] Due to the similarity between all the materials developed (V similar), α_m reflects the ease with which the local charge distribution (including dipoles) is distorted or reoriented by the applied electromagnetic field.

Hydrogen production by microwave-driven water splitting

The capacity of the materials to generate hydrogen using the microwave-driven water-splitting process was investigated in a fixed-bed quartz reactor within the microwave cavity described earlier. For this study, the materials were subjected to microwave irradiation while maintaining a flow of 100 mL min^{-1} of a 3 or 7% wet nitrogen atmosphere. Six cycles were conducted to obtain an average measurement of the oxygen and hydrogen produced. The mass spectrometer was calibrated using 5–10 mL pulses of different concentrations of O_2 and H_2 to accurately quantify the oxygen and hydrogen generated.

Results

Structural and textural characterization of La-doped ceria

A series of $Ce_{1-x}La_xO_{2-\delta}$ materials ($x = 0.05$–0.30) was synthesized by co-precipitation to investigate the impact of La^{3+} doping on microwave-driven redox behavior. Powder X-ray diffraction (XRD) confirmed that all compositions are single-phase cubic fluorite structured (Fm–3m) without detectable secondary phases (Fig. 1a). The substitution of Ce^{4+} (0.97 Å) with the larger La^{3+} cation (1.16 Å) resulted in a systematic shift of diffraction peaks to lower angles (Fig. 1b and S2(a–f)), indicating an expanded lattice. Rietveld refinement of the

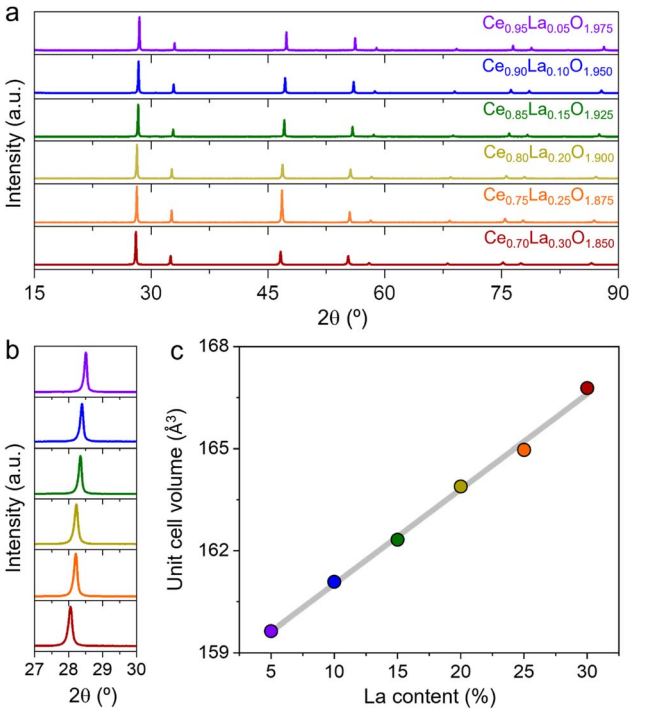

Fig. 1 Lanthanum doping expands the ceria lattice while preserving fluorite structure. (a) XRD patterns of $Ce_{1-x}La_xO_{2-\delta}$ ($x = 0.05$–0.30), all indexed to the fluorite phase; (b) zoom-in of primary diffraction peaks shows peak shifts with increasing La content; and (c) unit cell volume increases linearly with La content, confirming solid solution behavior by Vegard's law.

Open Access Article. Published on 10 maart 2026. Downloaded on 27-4-2026 02:35:05.
This article is licensed under a Creative Commons Attribution-NonCommercial 3.0 Unported Licence.

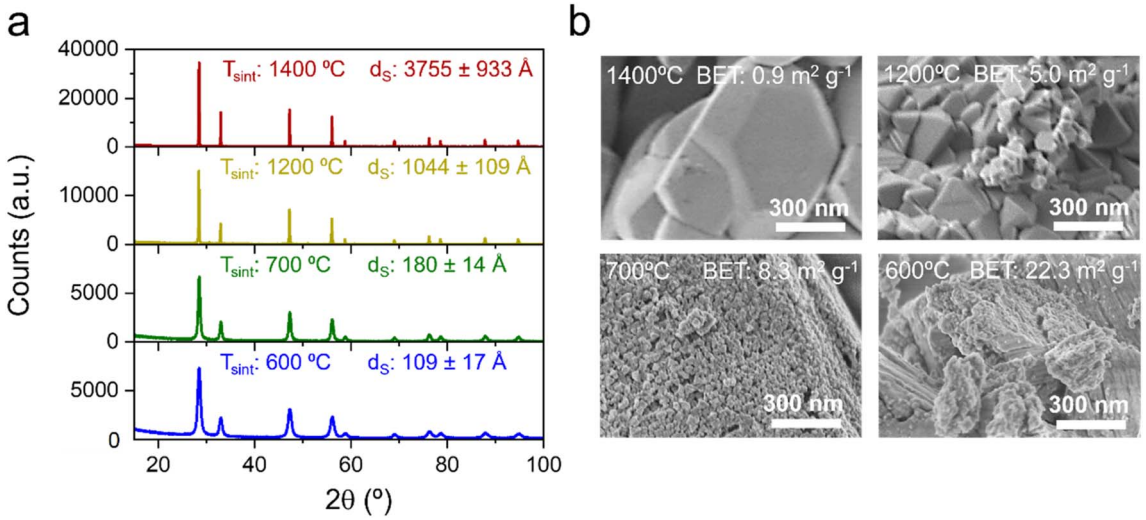

Fig. 2 Calcination temperature tunes grain size and surface area in $Ce_{0.9}La_{0.1}O_{2-\delta}$. (a) XRD and Scherrer analysis reveal decreasing crystallite size with lower calcination temperature; and (b) FESEM images and BET analysis show strong inverse relationship between particle size and surface area.

diffraction patterns showed a linear increase in unit cell volume with La content, in accordance with Vegard's law[39] (Fig. 1c), confirming homogeneous incorporation of La into the ceria lattice.

FESEM images of the synthesized samples (Fig. S3) revealed consistent microstructures with agglomerated primary fluorite crystallites in the 140–150 nm range. This morphological uniformity ensures that subsequent comparisons between samples are not influenced by surface area–related effects.[24,40] This point is critical, as variations in morphology could otherwise influence microwave absorption or redox kinetics *via* local field enhancements or surface diffusion processes.

To further decouple the role of microstructure from compositional effects, we focused on $Ce_{0.9}La_{0.1}O_{2-\delta}$ as the optimal formulation and prepared it at various calcination temperatures (600–1400 °C), thereby modulating its surface area and crystallinity. All samples retained the fluorite phase (Fig. 2a), but peak broadening and intensity changes confirmed smaller crystallite sizes at lower calcination temperatures, ranging from 3755 Å at 1400 °C to 109 Å at 600 °C, as estimated by the Scherrer equation. FESEM analysis (Fig. 2b) revealed significant coarsening at high temperatures, consistent with grain growth. The BET surface area declined exponentially from 22.3 to 0.9 $m^2\ g^{-1}$ across the temperature range, enabling a direct assessment of surface area effects on redox reactivity while maintaining fixed composition.

Influence of lanthanum concentration on dielectric polarization

The efficiency of microwave-driven reduction in oxides is governed not only by electronic conductivity but also by the material's ability to polarize under high-frequency electromagnetic fields. In ceria-based systems, polarization mechanisms include the orientation of lattice dipoles and the migration or

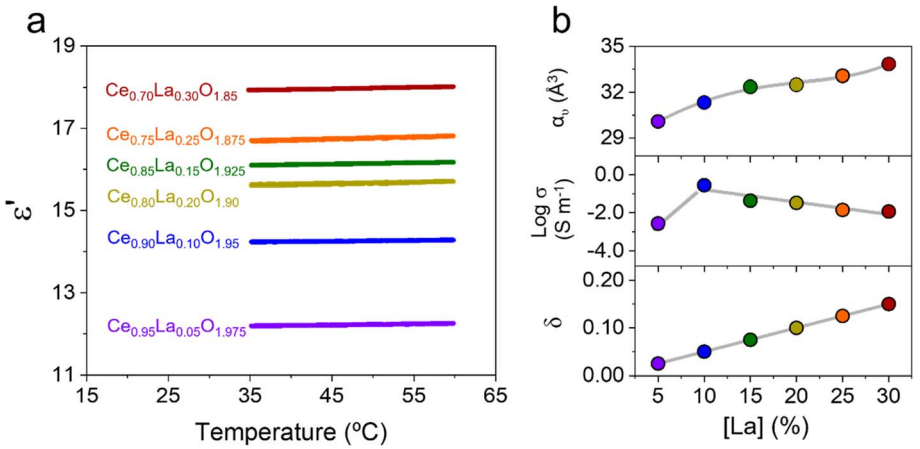

Fig. 3 Lanthanum doping enhances dielectric polarization through ionic and defect mechanisms. (a) Relative dielectric constant (ε') as a function of temperature for La-doped samples; (b) polarizability (α_υ), DC conductivity, and intrinsic $V_O^{\cdot\cdot}$ content (δ_{Ext}) *versus* La content, showing the decoupling between transport and dielectric response at high doping levels.

 This journal is © The Royal Society of Chemistry 2026

Open Access Article. Published on 10 maart 2026. Downloaded on 27-4-2026 02:35:05.
This article is licensed under a Creative Commons Attribution-NonCommercial 3.0 Unported Licence.

displacement of charge carriers, particularly oxygen ions and associated vacancies.[22,30,32,41,42] To elucidate how La doping affects this behavior, we analyzed the dielectric constant (ε') of the $Ce_{1-x}La_xO_{2-\delta}$ series at 50 °C under microwave excitation.

As shown in Fig. 3a, ε' increased with La content, ranging from 12 to 19 across the series. This enhancement correlates with the increased concentration of oxygen vacancies ($V_O^{\cdot\cdot}$) and local structural asymmetries induced by doping. Using these values, the polarizability volume (α_υ) was calculated and plotted alongside ionic conductivity (σ) and the extrinsic oxygen vacancy concentration (δ_{Ext}) (Fig. 3b). δ_{Ext} was estimated from charge balance calculations, assuming Ce^{4+} and La^{3+} oxidation states.

A noteworthy observation was the non-monotonic relationship between ionic conductivity (Fig. S5a) and La content, which peaked at 10 mol% La before declining.[43] This behavior suggests a trade-off, *i.e.*, while increasing La^{3+} introduces more $V_O^{\cdot\cdot}$ and enhances dielectric response, excessive doping promotes vacancy association, performing local order which reduces the mobility of O^{2-} ions. In contrast, α_υ followed a polynomial trend, increasing with La content and plateauing at high doping levels. This divergence indicates that polarization is not governed solely by mobile ions (orientation polarization) but also by intrinsic defect-related mechanisms.

Specifically, two types of polarization mechanisms can be identified: (1) orientation polarization,[22] associated with the displacement to opposite directions of O^{2-} ions and $V_O^{\cdot\cdot}$ under the microwave field, which dominates at low La contents and correlates with ionic conductivity; and (2) intrinsic or defect-driven polarization,[22,42] arising from $V_O^{\cdot\cdot}$–La^{3+} dipoles and localized charge carriers (*e.g.*, small polarons) trapped in asymmetric defect sites (*e.g.*, oxygen vacancies), which increase in importance at high doping levels.[21,32,44,45]

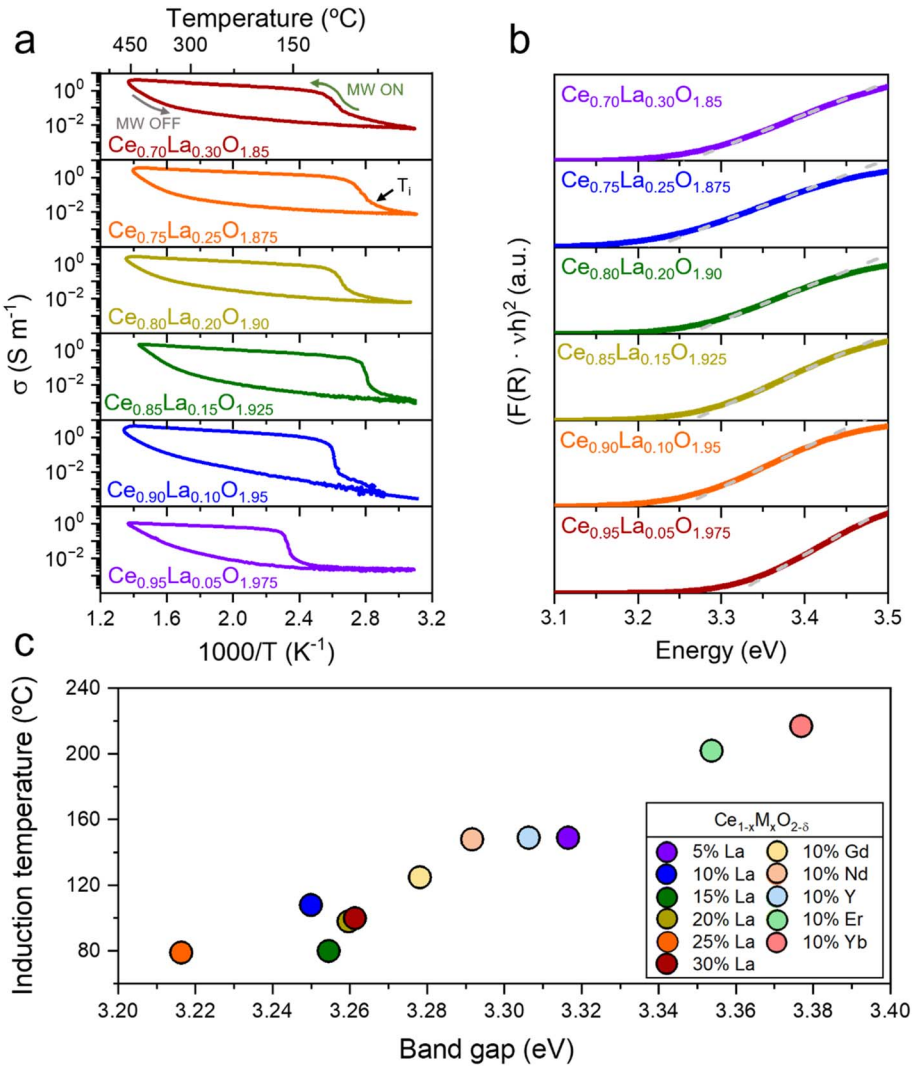

Fig. 4 Bandgap narrowing by La doping enables reduction at ultra-low temperatures. (a) *In situ* AC conductivity hysteresis subjected to 40–50 W g^{-1} microwave power in synthetic air during a redox cycle, and (b) optical bandgap determined by Kubelka–Munk plots reveals systematic bandgap reduction. The induction temperature (T_i) and band gap are the trend changes in conductivity at MW ON, and the energy value for $(F(R) \cdot vh)^2$ is equal to zero, respectively; (c) T_i scales linearly with bandgap across Ce-based oxides, establishing a predictive descriptor for microwave activation.

Open Access Article. Published on 10 maart 2026. Downloaded on 27-4-2026 02:35:05.
This article is licensed under a Creative Commons Attribution-NonCommercial 3.0 Unported Licence.

These findings reveal a critical mechanistic insight: enhanced microwave absorption in these oxides stems from the synergistic interplay between mobile ionic carriers and polarizable defect structures.[22] Importantly, while maximum conductivity occurs at 10% La, further increases in La content continue to enhance dielectric response *via* defect polarization, even if ionic mobility declines.[46] Modulating these characteristics enables the development of materials with a greater capacity to incorporate microwave-assisted energy, allowing them to reach T_i and P_{th} conditions using low power, avoiding excessive degradation of the material by such excess energy, ultimately increasing the overall energy efficiency of the process. This decoupling offers new strategies for optimizing microwave–matter interactions in non-metallic functional materials.

Effect of lanthanum doping on induction temperature and bandgap

The initiation of the redox process under microwave irradiation is triggered at the induction temperature (T_i), defined as the point at which electronic conductivity rises sharply, marking the onset of $Ce^{4+} \rightarrow Ce^{3+}$ reduction.[21,22,24] We monitored this transition *via in situ* conductivity measurements under microwave heating in synthetic air. T_i values ranged from 149 °C for $Ce_{0.95}La_{0.05}O_{2-\delta}$ to just 79 °C for $Ce_{0.75}La_{0.25}O_{2-\delta}$ (Fig. 4a), among the lowest reported for ceria-based redox systems.[22] This

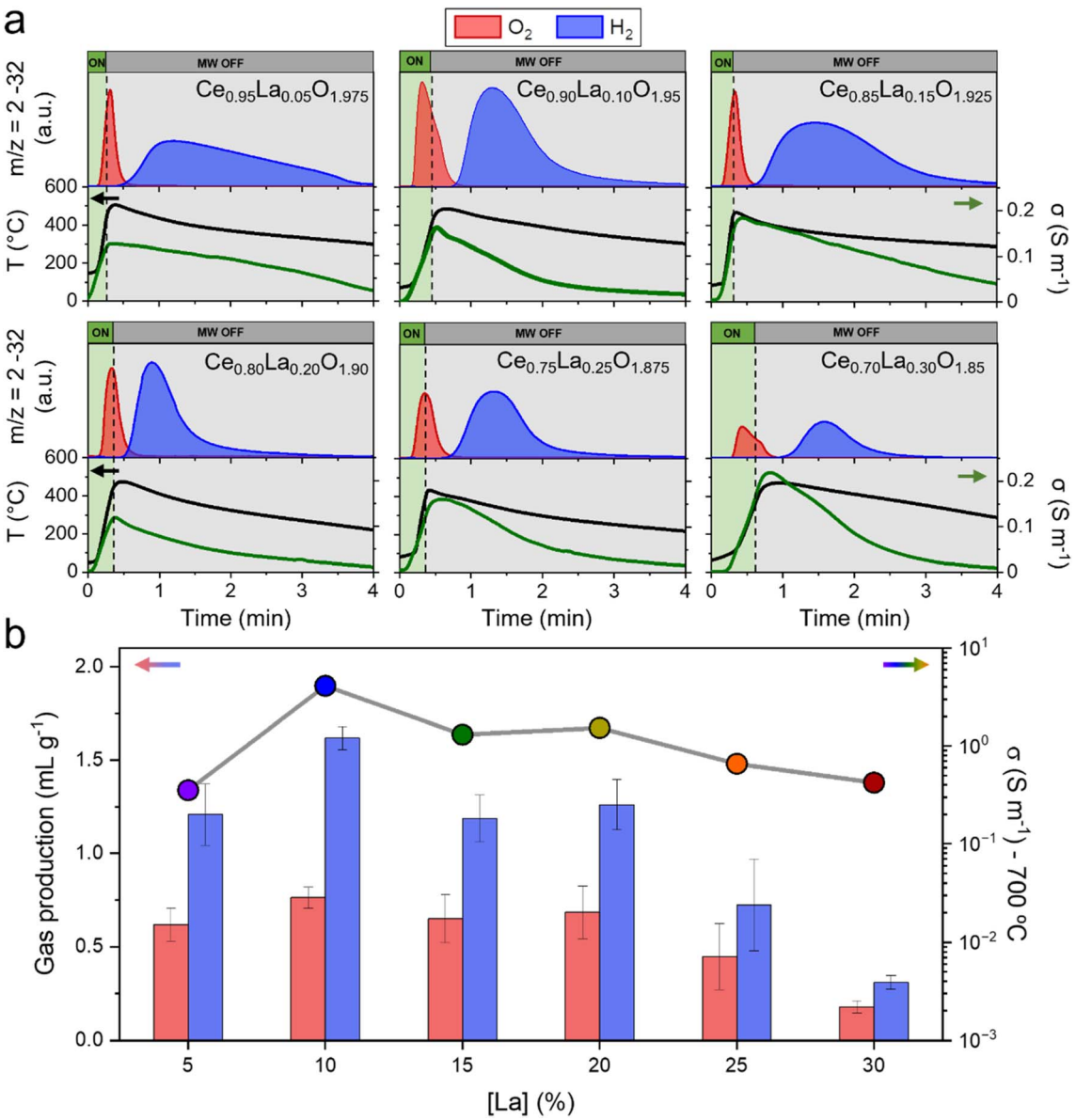

Fig. 5 Redox reactivity under microwave irradiation peaks at intermediate La content. (a) Representative water splitting cycle for oxygen carriers based on La-doped ceria ($Ce_{1-x}La_xO_{2-\delta}$) applying 40–50 W g^{-1} under wet N_2; and (b) total (O_2 and H_2) gas yield and DC conductivity at 700 °C in inert *versus* La content, showing a volcano-type trend with an optimum at 10% La.

 This journal is © The Royal Society of Chemistry 2026

Open Access Article. Published on 10 maart 2026. Downloaded on 27-4-2026 02:35:05.
This article is licensed under a Creative Commons Attribution-NonCommercial 3.0 Unported Licence.

behavior supports the hypothesis that La doping reduces the activation barrier for reduction.

To probe the electronic origins of this trend, we measured the optical bandgap of the materials using diffuse reflectance UV-vis spectroscopy. Kubelka–Munk plots showed a consistent decrease in bandgap energy from 3.32 eV to 3.21 eV as La content increased (Fig. 4b). This bandgap narrowing is attributed to lattice expansion,[20] enhanced orbital overlap, and the introduction of intermediate electronic states associated with defects and cation substitution.[24] Plotting T_i against bandgap energy revealed a strong linear correlation (Fig. 4c), establishing the bandgap as a predictive descriptor for the onset of reduction under microwave fields. This link was validated through our data and previous studies of doped ceria,[22] supporting a broadly-applicable mechanism primarily of electronic origin: the dopant-triggered orbital hybridization forms interbands that lower the energy threshold for excitation.[20,22] Consequently, narrower bandgaps facilitate faster electron promotion from the valence to the conduction band under microwave stimulation, leading to Ce^{4+} reduction at lower thermal loads.[22]

Post-reduction XRD and XPS analysis confirmed the reduction of Ce^{4+} to Ce^{3+} without structural degradation (Fig. S4a–c). The crystal structure remained intact, and gold internal standards ruled out instrumental artifacts. As illustrated in Fig. S4c, XPS spectra revealed signals corresponding to Ce^{4+} (at ~904 eV and 885 eV, associated with $3d_{3/2}$ and $3d_{5/2}$ orbitals, respectively) across all samples.[47,48] Upon microwave irradiation, distinct peaks assigned to Ce^{3+} appeared (at ~907 eV and 889 eV), confirming that cerium cations were partially reduced at low temperatures (~400 °C) under electromagnetic field exposure.[47,48] Notably, XPS spectra showed unchanged La^{3+} signals after microwave treatment, confirming that La acts as a passive dopant -facilitating electronic and structural changes without participating directly in the redox chemistry.[49,50] These results collectively demonstrate that La doping serves a dual function. It modulates the band structure to reduce the activation energy, facilitating the electron transition from O 2p to Ce 4f orbitals, which are involved in the reduction mechanism, thereby decreasing T_i.[22] Additionally, its incorporation in the ceria lattice increases defect concentration, enhancing microwave absorption *via* polarization.[22]

Kinetics and thermodynamics of microwave-driven water splitting

Having established the role of La in tuning polarization and electronic structure, we next evaluated its impact on redox kinetics and H_2 production. Microwave-assisted reduction-oxidation cycles were performed under a 3% H_2O/N_2 stream using a fixed-bed microwave cavity.[21,51] A representative cycle is shown in Fig. 5a. Upon reaching T_i, rapid reduction occurred within ~1 min, followed by reoxidation upon water exposure, releasing H_2. This fast, low-temperature cycling contrasts with conventional two-step redox cycles that typically operate above 1200 °C and require extended durations to reach equilibrium.[52] As shown in Fig. 5a and S6–S11, the onset of microwave-driven reduction is accompanied by a sharp increase in temperature and oxide-ion conductivity†, followed by oxygen release, Ce^{4+} reduction, and $V_O^{\cdot\cdot}$ formation in the lattice. The reduction stops once the material reaches ~400 °C, confirming that microwave fields enable rapid, low-temperature reduction of doped ceria far below conventional thermal thresholds.

Quantitative analysis of O_2 and H_2 yields over six cycles revealed a strong dependence on La content (Fig. 5b). $Ce_{0.9}La_{0.1}O_{2-\delta}$ showed the highest H_2 production (1.62 ± 0.06 mL g^{-1}), corresponding to O_2 evolution of 0.76 ± 0.06 mL g^{-1} ($\Delta\delta \sim 0.012$) and conductivity of 4.1 S m^{-1}. These values represent a balance between redox thermodynamics and kinetics:[53] low La content results in insufficient $V_O^{\cdot\cdot}$, limiting reduction, while high doping introduces thermodynamic barriers to further $V_O^{\cdot\cdot}$ formation due to defect association and higher δ_{Ext} values. This trend results in a volcano-type relationship between La content and both gas yields and conductivity (Fig. 5b), consistent with previous studies linking ionic conductivity to defect mobility in doped ceria systems.[22,24,25]

Importantly, all samples maintained a consistent ~2 : 1 H_2 : O_2 ratio, confirming high selectivity and complete water splitting. The deviation between gas production and conductivity at extreme doping levels suggests a complex interplay between mobility, $V_O^{\cdot\cdot}$ reactivity, and the enthalpy required to form new defects. For example, the 30% La-doped sample had sufficient conductivity (0.4 S m^{-1}) but the lowest gas output due to the thermodynamic cost of generating additional $V_O^{\cdot\cdot}$ beyond the high δ_{Ext} baseline. In contrast, the 5% sample exhibited low conductivity (0.3 S m^{-1}) but moderate gas production due to lower defect formation energy. This discrepancy highlights a critical factor: while ionic mobility is essential, the thermodynamics of oxygen release -intricately tied to δ_{Ext} – sets the ceiling for achievable $V_O^{\cdot\cdot}$ concentration‡ during microwave reduction.[54] As illustrated in Fig. 3b, increasing La doping raises δ_{Ext}, which in turn increases the energy required for the further formation of extrinsic $V_O^{\cdot\cdot}$. Thus, materials with excessive pre-existing vacancies become thermodynamically resistant to further reduction under a fixed energy input.

This behavior was further confirmed by oxidation kinetics, which also varied with La content. The time required for full reoxidation ranged from 4 min for $Ce_{0.95}La_{0.05}O_{2-\delta}$ to 2 min for $Ce_{0.9}La_{0.1}O_{2-\delta}$ (Fig. S6–S11), reinforcing the role of ionic mobility as a rate-limiting step in surface water splitting. The shorter oxidation times observed for 10% La doping indicate a more favorable kinetic regime, likely due to faster diffusion of surface-adsorbed species into the bulk oxide. Furthermore, unlike Mn-doped perovskites,[25] which often exhibit a transient performance decay due to initial sintering, the La-doped ceria system demonstrates sustained stability over 20 redox cycles without structural degradation.[22] Regarding other lanthanide

† To confirm this, the conductivity was measured by the DC method in an inert atmosphere (Fig. S5b), which is reported that corresponds to a predominantly ionic conductivity.[32]

‡ In the case of cerium oxides, when the material reaches a δ_{Int} of 0.17 ($CeO_{1.83}$), decomposition begins, forming Ce^{3+} oxides. These oxides strongly stabilize Ce^{3+}, not the water splitting process by oxidation to Ce^{4+}.[54]

Open Access Article. Published on 10 maart 2026. Downloaded on 27-4-2026 02:35:05.
This article is licensed under a Creative Commons Attribution-NonCommercial 3.0 Unported Licence.

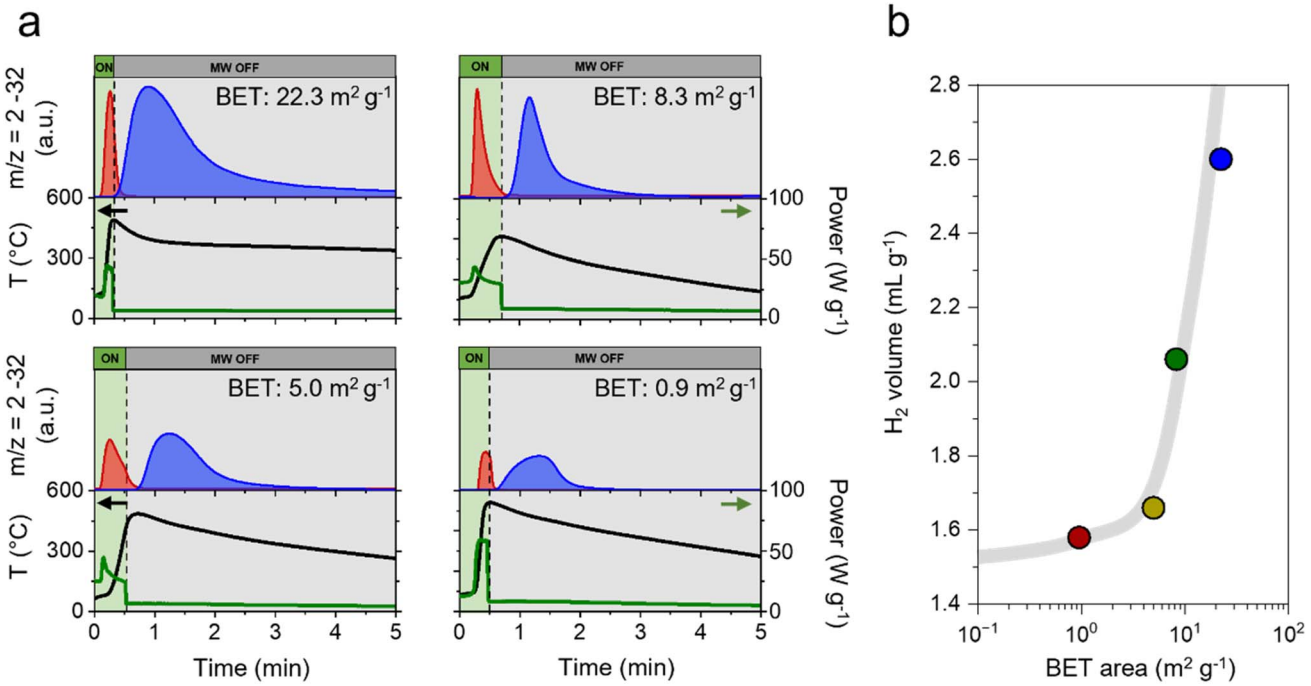

Fig. 6 Surface area amplifies hydrogen production in $Ce_{0.9}La_{0.1}O_{1.95}$. (a) H_2 and O_2 evolution profiles during microwave-driven water splitting cycles for samples with varying surface areas (samples sintered at 700, 900, 1200, and 1400 °C); (b) variation of the amount of H_2 produced with respect to the BET area.

dopants, La has shown a superior performance in the production of oxygen and subsequent hydrogen generation.[22]

These findings validate a key mechanistic insight: the optimal redox activity in microwave-driven ceria systems arises from a delicate balance between oxygen-ion mobility and the energy landscape for $V_O^{\cdot\cdot}$ formation. La doping offers a means to tune both parameters, with 10% providing the best trade-off. This dual control over kinetics and thermodynamics enables materials such as $Ce_{0.9}La_{0.1}O_{2-\delta}$ to operate with both high energy-conversion rate and low energy input, paving the way for scalable, electrified hydrogen production.

Surface area enhances productivity but limits long-term stability

Finally, we investigated how tuning surface area impacts fuel productivity in the best-performing composition, $Ce_{0.9}La_{0.1}O_{2-\delta}$. Samples calcined at different temperatures (600–1400 °C) offered a range of BET areas from 0.9 to 22.3 $m^2\ g^{-1}$. Redox cycling revealed a strong positive correlation between surface area and gas output (Fig. 6a). The highest-area sample produced 2.60 mL g^{-1} H_2 and 1.31 mL g^{-1} O_2, exceeding previously reported values for $Ce_{0.8}Gd_{0.2}O_{1.9}$ at similar surface areas.[24] This notable enhancement arises from the combination of La-induced ionic conductivity and increased oxygen availability, which allows deeper – grain interior-lattice oxygen to participate in the reduction process compared to Gd-doped analogues.

Plotting H_2 yield against BET area showed an exponential trend (Fig. 6b), underscoring the importance of surface exchange kinetics during rapid redox transitions. As previously reported,[24] the reduction primarily occurs at the grain surface, where lattice oxygen is less tightly bound. Therefore, lattice reduction is favored by decreasing particle size and increasing the specific surface area. Smaller particles allow for shorter diffusion pathways *via* oxygen vacancies, ensuring ions are evacuated efficiently instead of recombining within the bulk lattice. Indeed, FESEM analysis revealed that reducing crystallite size from ~862 nm (sintered at 1400 °C) to ~26 nm (sintered at 600 °C) dramatically reduced the $V_O^{\cdot\cdot}$ diffusion length toward the grain surface, enhancing accessible surface oxygen (Fig. 2b). This trend highlights the synergy between nanoscale grains, microwave-induced electronic polarization, and accelerated water dissociation kinetics at defect-rich surfaces.

However, multicycle testing uncovered trade-offs in durability. As shown in Fig. 7, materials with high surface area experienced a gradual decline in H_2 production over six cycles, attributed to microwave-induced sintering and grain growth (confirmed by FESEM, Fig. S12). Lower-temperature-sintered samples showed more significant coarsening, leading to reduced active area and performance loss. For example, the high-surface-area sample (22.3 $m^2\ g^{-1}$) decreased from 2.62 to ~2.04 mL g^{-1} H_2 over six cycles, while the low-surface-area sample (0.9 $m^2\ g^{-1}$) declined slightly from 1.58 to 1.51 mL g^{-1}.

Interestingly, FESEM (Fig. S12) showed that the 8.3 $m^2\ g^{-1}$ sample suffered the most severe particle coarsening, whereas the 22.3 $m^2\ g^{-1}$ sample exhibited less agglomeration and maintained stable productivity beyond the third cycle. This counterintuitive trend highlights the role of initial microstructure in governing long-term durability, suggesting that tailored porosity and crystallite connectivity can mitigate microwave-induced sintering.

 This journal is © The Royal Society of Chemistry 2026

Open Access Article. Published on 10 maart 2026. Downloaded on 27-4-2026 02:35:05.
This article is licensed under a Creative Commons Attribution-NonCommercial 3.0 Unported Licence.

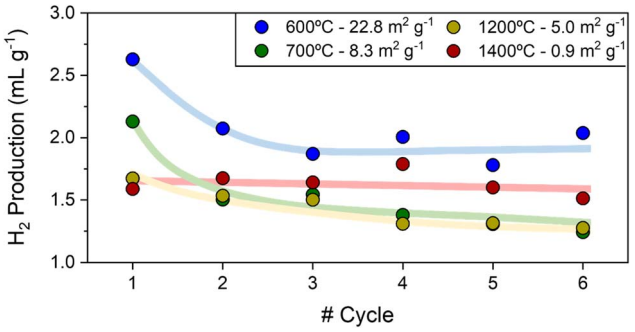

Fig. 7 Hydrogen production stability varies with surface area under repeated cycling. Hydrogen production by microwave-assisted water splitting over 6 cycles for $Ce_{0.9}La_{0.1}O_{2-\delta}$ material with variable surface area in an atmosphere of 100 mL min^{-1} wet N_2 at 7%. Higher surface areas promote initial productivity gains but suffer more degradation, while low-area samples achieve stable performance over six cycles.

These results highlight that while surface area is critical for maximizing H_2 output, it must be optimized alongside thermal and structural stability. Future efforts may focus on incorporating thermally-stable porous structures or dopants that inhibit sintering under microwave fields, such as cross-linked oxide scaffolds or doped mesoporous matrices. Overall, our findings demonstrate that three parameters must be co-optimized, *i.e.* ionic conductivity in reducing conditions, availability of oxygen, and textural properties (crystallite size and surface area), to design next-generation materials capable of delivering both high hydrogen productivity and structural resilience during repeated microwave-driven redox cycles.

Conclusions

This study elucidates the fundamental role of lanthanum doping in modulating the redox behavior of ceria-based oxides ($Ce_{1-x}La_xO_{2-\delta}$) under microwave-assisted thermochemical cycling. By systematically varying La content ($x = 0.05$–0.30), we demonstrate that dielectric polarization in these materials arises not only from ionic conductivity but also from the presence and polarizability of intrinsic oxygen vacancies. This dual mechanism underpins the enhanced microwave absorption and redox reactivity observed.

Importantly, the induction temperature (T_i) of each material was found to correlate directly with its optical bandgap, independent of dopant concentration, confirming that electronic structure – rather than absolute defect density – governs the onset of reduction. This correlation holds across different ceria-based systems, establishing the bandgap as a reliable predictor for microwave-driven redox initiation.

In terms of hydrogen production, $Ce_{0.9}La_{0.1}O_{1.95}$ emerged as the optimal formulation, achieving 1.62 ± 0.06 mL g^{-1} of H_2 per cycle. When textural properties were tuned to increase surface area, hydrogen output rose exponentially, peaking at 2.60 mL g^{-1} for a BET area of 22.3 m^2 g^{-1}. However, durability tests revealed that high-surface-area, nano-grained samples suffered from microwave-induced sintering and initial performance decay, although maintained stable H_2 yields around 2.0 mL g^{-1} across multiple cycles. This highlights the critical trade-off between maximizing productivity and ensuring long-term structural resilience under repeated operation.

Overall, these results highlight that optimizing microwave-active redox materials requires a triad of strategies: electronic structure engineering to minimize T_i, defect chemistry to balance ionic mobility and vacancy reactivity, and microstructural design to couple high surface accessibility with stability against coarsening. This integrated approach provides a robust pathway for advancing scalable, low-temperature hydrogen production technologies.

Conflicts of interest

There are no conflicts to declare.

Data availability

The data supporting this article have been included as part of the supplementary information (SI). Supplementary information is available. See DOI: https://doi.org/10.1039/d5ta07647a.

Acknowledgements

Financial support by the Spanish Ministry of Science and Innovation and European Union (TED2021-132590B-C22, NextGenerationEU/PRTR, PID2022-139663OB-100, and CEX2021-001230-S grants funded by MCIN/AEI/10.13039/501100011033, "Ramon y Cajal" Fellowship RYC2021-033889-I grants) and Vice-Rectorate for Research of the Universitat Politècnica de València (PAID-06-24 grants). Also, we acknowledge the support of the Servicio de Microscopía Electrónica of the UPV.

References

1 N. Abas, A. Kalair and N. Khan, Review of Fossil Fuels and Future Energy Technologies, *Futures*, 2015, **69**, 31–49, DOI: 10.1016/j.futures.2015.03.003.
2 R. Schäppi, D. Rutz, F. Dähler, A. Muroyama, P. Haueter, J. Lilliestam, A. Patt, P. Furler and A. Steinfeld, Drop-in Fuels from Sunlight and Air, *Nature*, 2022, **601**(7891), 63–68, DOI: 10.1038/s41586-021-04174-y.
3 M. Sjardin, K. J. Damen and A. P. C. Faaij, Techno-Economic Prospects of Small-Scale Membrane Reactors in a Future Hydrogen-Fuelled Transportation Sector, *Energy*, 2006, **31**(14), 2523–2555, DOI: 10.1016/j.energy.2005.12.004.
4 M.-R. Valladares, *Global Trends and Outlook for Hydrogen. IEA Hydrogen*, 2017.
5 E. Stefan, B. Talic, Y. Larring, A. Gruber and T. A. Peters, Materials Challenges in Hydrogen-Fuelled Gas Turbines, *Int. Mater. Rev.*, 2022, **67**(5), 461–486, DOI: 10.1080/09506608.2021.1981706.
6 J. Incer-Valverde, A. Korayem, G. Tsatsaronis and T. Morosuk, "Colors" of Hydrogen: Definitions and Carbon Intensity, *Energy Convers. Manage.*, 2023, **291**, 117294, DOI: 10.1016/j.enconman.2023.117294.

Open Access Article. Published on 10 maart 2026. Downloaded on 27-4-2026 02:35:05. This article is licensed under a Creative Commons Attribution-NonCommercial 3.0 Unported Licence.

7 Q. Hassan, S. Algburi, A. Z. Sameen, H. M. Salman and M. Jaszczur, Green Hydrogen: A Pathway to a Sustainable Energy Future, *Int. J. Hydrogen Energy*, 2024, **50**, 310–333, DOI: 10.1016/j.ijhydene.2023.08.321.

8 C. Ortiz, C. Tejada, R. Chacartegui, R. Bravo, A. Carro, J. M. Valverde and J. Valverde, Solar Combined Cycle with High-Temperature Thermochemical Energy Storage, *Energy Convers. Manage.*, 2021, **241**, 114274, DOI: 10.1016/j.enconman.2021.114274.

9 V. K. Budama, J. P. Rincon Duarte, M. Roeb and C. Sattler, Potential of Solar Thermochemical Water-Splitting Cycles: A Review, *Sol. Energy*, 2023, **249**, 353–366, DOI: 10.1016/j.solener.2022.11.001.

10 B. Bulfin, M. Lange, L. de Oliveira, M. Roeb and C. Sattler, Solar Thermochemical Hydrogen Production Using Ceria Zirconia Solid Solutions: Efficiency Analysis, *Int. J. Hydrogen Energy*, 2016, **41**(42), 19320–19328, DOI: 10.1016/j.ijhydene.2016.05.211.

11 S. Padula, C. Tregambi, M. Troiano, A. Di Benedetto, P. Salatino, G. Landi and R. Solimene, Chemical Looping Reforming with Perovskite-Based Catalysts for Thermochemical Energy Storage, *Energies*, 2022, **15**(22), 8556, DOI: 10.3390/en15228556.

12 A. H. Bork, E. Povoden-Karadeniz, A. J. Carrillo and J. L. M. Rupp, Thermodynamic Assessment of the Solar-to-Fuel Performance of $La_{0.6}Sr_{0.4}Mn_{1-y}Cr_yO_{3-\delta}$ Perovskite Solid Solution Series, *Acta Mater.*, 2019, **178**, 163–172, DOI: 10.1016/j.actamat.2019.07.022.

13 A. J. Carrillo, A. H. Bork, T. Moser, E. Sediva, Z. D. Hood and J. L. M. Rupp, Modifying $La_{0.6}Sr_{0.4}MnO_3$ Perovskites with Cr Incorporation for Fast Isothermal CO_2-Splitting Kinetics in Solar-Driven Thermochemical Cycles, *Adv. Energy Mater.*, 2019, **178**, 163–172, DOI: 10.1002/aenm.201803886.

14 A. H. Bork, A. J. Carrillo, Z. D. Hood, B. Yildiz and J. L. M. Rupp, Oxygen Exchange in Dual-Phase $La_{0.65}Sr_{0.35}MnO_{3-\delta}$-$CeO_2$ Composites for Solar Thermochemical Fuel Production, *ACS Appl. Mater. Interfaces*, 2020, **12**(29), 32622–32632, DOI: 10.1021/acsami.0c04276.

15 R. B. Harikrishna, S. Sharma, H. Deka, T. Sundararajan and G. Ranga Rao, Thermochemical Production of Green Hydrogen Using Ferrous Scrap Materials, *Int. J. Hydrogen Energy*, 2024, **52**, 1488–1497, DOI: 10.1016/j.ijhydene.2023.08.070.

16 J. E. Lee, I. Shafiq, M. Hussain, S. S. Lam, G. H. Rhee and Y. K. Park, A Review on Integrated Thermochemical Hydrogen Production from Water, *Int. J. Hydrogen Energy*, 2022, **47**(7), 4346–4356, DOI: 10.1016/j.ijhydene.2021.11.065.

17 M. Ezbiri, K. M. Allen, M. E. Gàlvez, R. Michalsky and A. Steinfeld, Design Principles of Perovskites for Thermochemical Oxygen Separation, *ChemSusChem*, 2015, **8**(11), 1966–1971, DOI: 10.1002/cssc.201500239.

18 S. Bhavsar, N. Isenberg, A. More and G. Veser, Lanthana-Doped Ceria as Active Support for Oxygen Carriers in Chemical Looping Combustion, *Appl. Energy*, 2016, **168**, 236–247, DOI: 10.1016/j.apenergy.2016.01.073.

19 E. Sediva, A. J. Carrillo, C. E. Halloran and J. L. M. Rupp, Evaluating the Redox Behavior of Doped Ceria for Thermochemical CO_2 Splitting Using Time-Resolved Raman Spectroscopy, *ACS Appl. Energy Mater.*, 2021, **4**(2), 1474–1483, DOI: 10.1021/acsaem.0c02675.

20 C. Muhich and A. Steinfeld, Principles of Doping Ceria for the Solar Thermochemical Redox Splitting of H_2O and CO_2, *J. Mater. Chem. A*, 2017, **5**(30), 15578–15590, DOI: 10.1039/C7TA04000H.

21 J. M. Serra, J. F. Borrás-Morell, B. García-Baños, M. Balaguer, P. Plaza-González, J. Santos-Blasco, D. Catalán-Martínez, L. Navarrete and J. M. Catalá-Civera, Hydrogen Production *via* Microwave-Induced Water Splitting at Low Temperature, *Nat. Energy*, 2020, **5**, 910–919, DOI: 10.1038/s41560-020-00720-6.

22 A. Domínguez-Saldaña, L. Navarrete, M. Balaguer, A. J. Carrillo, J. Santos, B. García-Baños, P. Plaza-González, D. Catalán-Martínez, J. M. Catalá-Civera and J. M. Serra, Enhanced Hydrogen Production in Microwave-Driven Water-Splitting Redox Cycles by Engineering Ceria Properties, *Adv. Energy Mater.*, 2024, **14**, 2401443, DOI: 10.1002/aenm.202401443.

23 A. López-García, A. Domínguez-Saldaña, A. J. Carrillo, L. Navarrete, M. I. Valls, B. García-Baños, P. J. Plaza-Gonzalez, J. M. Catala-Civera and J. M. Serra, Microwave-Driven Exsolution of Ni Nanoparticles in A-Site Deficient Perovskites, *ACS Nano*, 2023, **17**(23), 23955–23964, DOI: 10.1021/acsnano.3c08534.

24 J. M. Serra, M. Balaguer, J. Santos-Blasco, J. F. Borras-Morell, B. Garcia-Baños, P. Plaza-Gonzalez, D. Catalán-Martínez, F. Penaranda-Foix, A. Domínguez, L. Navarrete and J. M. Catala-Civera, Modulating Redox Properties of Solid-State Ion-Conducting Materials Using Microwave Irradiation, *Mater. Horiz.*, 2023, **10**, 5796–5804, DOI: 10.1039/D3MH01339A.

25 A. Domínguez-Saldaña, A. J. Carrillo, M. Balaguer, L. Navarrete, J. Santos, D. Catalán-Martínez, B. García-Baños, P. J. Plaza-González, J. D. Gutierrez-Cano, F. Peñaranda, J. M. Catalá-Civera and J. M. Serra, Microwave-Driven Reduction Accelerates Oxygen Exchange in Perovskite Oxides, *ACS Appl. Mater. Interfaces*, 2024, **16**, 69324–69332, DOI: 10.1021/acsami.4c15150.

26 J. Zhao, D. Wang, L. Zhang, M. He, W. Ma and S. Zhao, Microwave-Enhanced Hydrogen Production: A Review, *RSC Adv.*, 2023, **13**(22), 15261–15273, DOI: 10.1039/D3RA01898A.

27 M. Taeño, F. Torre, A. M. Huerta-Flores, C. Luengo, A. Azpiazu, E. P. Del Barrio and S. Doppiu, Microwave-Induced Hydrogen Production at Medium Temperature of Iron Oxide/Hercynite Composite, *Int. J. Hydrogen Energy*, 2025, **97**, 718–726, DOI: 10.1016/J.IJHYDENE.2024.11.476.

28 C. Wang, S. Sourav, K. Yu, Y. Kwak, W. Zheng and D. G. Vlachos, Green Syngas Production by Microwave-Assisted Dry Reforming of Methane on Doped Ceria Catalysts, *ACS Sustain. Chem. Eng.*, 2023, **11**, 13353–13362, DOI: 10.1021/acssuschemeng.3c02693.

29 C. W. M. Castleton, A. L. Lee, J. Kullgren, and K. Hermansson, Description of Polarons in Ceria Using

 This journal is © The Royal Society of Chemistry 2026

Open Access Article. Published on 10 maart 2026. Downloaded on 27-4-2026 02:35:05.
This article is licensed under a Creative Commons Attribution-NonCommercial 3.0 Unported Licence.

Density Functional Theory, in *Journal of Physics: Conference Series*, Institute of Physics Publishing, 2014, vol. 526, DOI: 10.1088/1742-6596/526/1/012002.

30 M. Balaguer, C. Y. Yoo, H. J. M. Bouwmeester and J. M. Serra, Bulk Transport and Oxygen Surface Exchange of the Mixed Ionic-Electronic Conductor $Ce_{1-x}Tb_xO_{2-\delta}$ (x = 0.1, 0.2, 0.5), *J. Mater. Chem. A*, 2013, **1**(35), 10234–10242, DOI: 10.1039/c3ta11610g.

31 M. Nagao, T. Kimura, Y. Kio Mizuno, M. Kosa and M. Leda, Detection of Joule Heating before Dielectric Breakdown in Polyethylene Films, *IEEE Trans. Electr.*, 1990, **25**(4), 715–722.

32 M. Balaguer, C. Solís and J. M. Serra, Structural-Transport Properties Relationships on $Ce_{1-x}Ln_xO_{2-\delta}$ System (Ln = Gd, La, Tb, Pr, Eu, Er, Yb, Nd) and Effect of Cobalt Addition, *J. Phys. Chem. C*, 2012, **116**, 7975–7982, DOI: 10.1021/jp211594d.

33 A. Ismail, J. Hooper, J. B. Giorgi and T. K. Woo, A DFT+U Study of Defect Association and Oxygen Migration in Samarium-Doped Ceria, *Phys. Chem. Chem. Phys.*, 2011, **13**(13), 6116–6124, DOI: 10.1039/c0cp02062a.

34 T. C. Davenport, M. Kemei, M. J. Ignatowich and S. M. Haile, Interplay of Material Thermodynamics and Surface Reaction Rate on the Kinetics of Thermochemical Hydrogen Production, *Int. J. Hydrogen Energy*, 2017, **42**(27), 16932–16945, DOI: 10.1016/j.ijhydene.2017.05.184.

35 D. Röhrens, M. Runde, R. A. De Souza, and U. Simon *On the Microwave-Heating Behavior of Acceptor- and Donor-Type Substituted CeO2*, 2025, DOI: 10.26434/CHEMRXIV-2025-5GZC7.

36 F. T. L. Muniz, M. A. R. Miranda, C. Morilla Dos Santos and J. M. Sasaki, The Scherrer Equation and the Dynamical Theory of X-Ray Diffraction, *Acta Crystallogr., Sect. A:Found. Adv.*, 2016, **72**(3), 385–390, DOI: 10.1107/S205327331600365X.

37 J. Shanker, and S. Dixit, *Dielectric Constants and Their Pressure and Temperature Derivatives for Ionic Crystals*, 1991, vol. 123.

38 A. J. Boslkan and A. E. E. Havinga, Temperature Dependence of Dielectric Constants of Cubic Ionic Comyounds, *Phys. Rev.*, 1963, **1269**, 1593–1600, DOI: 10.1103/PhysRev.129.1593.

39 L. Vegard, Die Konstitution Der Mischkristalle Und Die Raumfüllung Der Atome, *Z. Phys.*, 1921, **5**(1), 17–26, DOI: 10.1007/BF01349680.

40 R. Khrapko *Polarization Energy of a Dielectric*. 2008.

41 M. Balaguer, New Solid State Oxygen and Hydrogen Conducting Materials, *Towards Their Applications as High Temperature Electrochemical Devices and Gas Separation Membranes*, 2013.

42 C. Gong, J. Ding, C. Wang, Y. Zhang, Y. Guo, K. Song, C. Shi and F. He, Defect-Induced Dipole Polarization Engineering of Electromagnetic Wave Absorbers: Insights and Perspectives, *Composites, Part B*, 2023, **252**, 110479, DOI: 10.1016/j.compositesb.2022.110479.

43 J. Zamudio-García, J. M. Porras-Vázquez, J. Canales-Vázquez, A. Cabeza, E. R. Losilla and D. Marrero-López, Relationship between the Structure and Transport Properties in the $Ce_{1-x}La_xO_{2-x/2}$ System, *Inorg. Chem.*, 2019, **58**(14), 9368–9377, DOI: 10.1021/ACS.INORGCHEM.9B01104/SUPPL_FILE/IC9B01104_SI_001.PDF.

44 C. Steiner, A. M. Gänzler, M. Zehentbauer, G. Hagen, M. Casapu, S. Müller, J. D. Grunwaldt and R. Moos, Oxidation State and Dielectric Properties of Ceria-Based Catalysts by Complementary Microwave Cavity Perturbation and X-Ray Absorption Spectroscopy Measurements, *Top. Catal.*, 2019, **62**(1–4), 227–236, DOI: 10.1007/s11244-018-1110-3.

45 T. Zhu, J. Liu, Q. Wang, X. Zhu and B. Sun, Enhanced Hydrogen Production by Microwave Liquid-Phase Discharge Plasma Reforming of Methanol Solution without Catalyst, *J. Energy Inst.*, 2023, **108**, 101246, DOI: 10.1016/j.joei.2023.101246.

46 Z.-P. Li, T. Mori, J. Zou and J. Drennan, Defects Clustering and Ordering in Di- and Trivalently Doped Ceria, *Mater. Res. Bull.*, 2013, **48**(2), 807–812, DOI: 10.1016/j.materresbull.2012.11.073.

47 K. I. Maslakov, Y. A. Teterin, A. J. Popel, A. Y. Teterin, K. E. Ivanov, S. N. Kalmykov, V. G. Petrov, P. K. Petrov and I. Farnan, XPS Study of Ion Irradiated and Unirradiated CeO_2 Bulk and Thin Film Samples, *Appl. Surf. Sci.*, 2018, **448**, 154–162, DOI: 10.1016/j.apsusc.2018.04.077.

48 G. M. Iogo, E. Paparazzo, C. Nazionale delle Ricerche, pz le Aldo Moro and I. N. Zacchetti, XPS Studies on Cerium, Zirconium and Yttrium Valence States in Plasma-Sprayed Coatings 0. Bagnarelli, *Surf. Interface Anal.*, 1990, **16**, 515–519, DOI: 10.1002/sia.7401601107.

49 J. F. Moulder, W. F. Stickle, P. E. Sobol, K. D. Bomen and J. Chastain, *Reference Book of Standard Spectra for Identification and Interpretation of XPS Data*, 1992.

50 J. F. Moulder, J. Chastain, and R. C. King, *Handbook of X-Ray Photoelectron Spectroscopy : A Reference Book of Standard Spectra for Identification and Interpretation of XPS Data; Physical Electronics*, 1995.

51 M. Levy, and J. Fouletier, *Influence Of Dopant Concentration On The Electronic Conductivity Of Nonstoichiometric Y'itria-Doped Ceria*, 1984, vol. 12.

52 Y. Hao, C. K. Yang and S. M. Haile, High-Temperature Isothermal Chemical Cycling for Solar-Driven Fuel Production, *Phys. Chem. Chem. Phys.*, 2013, **15**(40), 17084–17092, DOI: 10.1039/c3cp53270d.

53 M. Laqdiem, A. J. Carrillo, G. Dimitrakopoulos, M. Balaguer, J. Garcia-Fayos, A. F. Ghoniem and J. M. Serra, Impact of Lattice Properties on the CO_2 Splitting Kinetics of Lanthanide-Doped Cerium Oxides for Chemical Looping Syngas Production, *Solid State Ionics*, 2023, **394**, 116192, DOI: 10.1016/j.ssi.2023.116192.

54 V. Perrichon, A. Laachir, G. Bergeret, R. Frety and L. Tournayan, Reduction of Cerias with Different Textures by Hydrogen and Their Reoxidation by Oxygen, *J. Chem. Soc., Faraday Trans.*, 1994, **40**, 773–781.